

Topical Perspectives

Effects of the central potassium ions on the G-quadruplex and stabilizer binding

Zhiguo Wang^{a,*}, Jun-Ping Liu^{a,b,c,d,**}^a Institute of Aging Research, School of Medicine, Hangzhou Normal University, Hangzhou, Zhejiang Province 311121, China^b Department of Immunology, Central Eastern Clinical School, Monash University, Melbourne, Victoria 3004, Australia^c Hudson Institute of Medical Research, Clayton, Victoria 3168, Australia^d Department of Molecular and Translational Science, Monash University, Clayton, Victoria 3168, Australia

ARTICLE INFO

Article history:

Received 25 September 2016

Received in revised form

20 December 2016

Accepted 4 January 2017

Available online 6 January 2017

Keywords:

G-Quadruplex

Potassium ion

Binding process

Binding free energy

ABSTRACT

Human telomeres undertake the structure of intra-molecular parallel G-quadruplex in the presence of K⁺ in eukaryotic cell. Stabilization of the telomere G-quadruplex represents a potential strategy to prevent telomere lengthening by telomerase in cancer therapy. Current work demonstrates that the binding of central K⁺ with the parallel G-quadruplex is a coordinated water directed step-wise process. The K⁺ above the top G-tetrad is prone to leak into environment and the 5'-adenine quickly flips over the top G-tetrad, leading to the bottom gate of G-tetrads as the only viable pathway of K⁺ binding. Present molecular dynamics studies on the two most potent stabilizers RHPS4 and BRACO-19 reveal that the central K⁺ has little influence on the binding conformations of the bound stabilizers. But without the central K⁺, either RHPS4 or BRACO-19 cannot stabilize the structure of G-quadruplex. The binding strength of stabilizers evaluated by the MM-PBSA method follows the order of BRACO-19 > RHPS4, which agrees with the experimental results. The difference in binding affinities between RHPS4 and BRACO-19 is probably related to the ability to form intramolecular hydrogen bonds and favorable van der Waals interactions with G-quadruplex. In the models that have one central K⁺ located at the upper/lower binding site, the corresponding top/bottom stacked stabilizers show more favorable binding affinities, indicating the apparent promoting effect of central K⁺ on the stabilizer binding. Our findings provide further insights into the regulatory effect of K⁺ on the G-quadruplex targeted binding, which is meaningful to the development of G-quadruplex stabilizers.

© 2017 Elsevier Inc. All rights reserved.

1. Introduction

G-Quadruplexes are high-order nucleic acid structures in guanine-rich regions such as telomeres [1–3], the promoter regions of proto-oncogene c-myc [4], c-kit [5] and bcl2 [6,7], and untranslated regions of mRNAs. [8,9] Bioinformatics analysis indicates that there are ~400,000 putative G-quadruplex-forming sequences in the human genome [10]. Human telomeres located at the very end of chromosomes are double-stranded DNAs ([T₂AG₃/C₃TA₂]_n) for most of its length with a terminal single-stranded overhang of 100–200 bases ([T₂AG₃]_n) [11]. Under physiological conditions, the telomere overhang bases are predicted to form intra-molecular

G-quadruplexes that are recognized as potential target for cancer therapy by inhibiting telomerase activity in most cancers [12,13].

The structures of human telomeric G-quadruplexes include three parts, i.e. the layers of rigid coplanar guanine tetrad (G-tetrad) holding together through Hoogsteen hydrogen bonds, the flexible TTA linking loops and the central alkali metal ions. Being polymorphic in structure, G-quadruplexes differ in their loop and tetrad arrangements, strand orientation and capping structures. Most G-quadruplexes show parallel, antiparallel, hybrid-I and hybrid-II conformations that are not constant but undergo conversions from one type to another when the environmental metal cations (K⁺ or Na⁺) changes [14].

The X-ray and NMR analysis on G-quadruplex–ligand complexes have identified various small molecules that specifically induce and stabilize G-quadruplexes, including acridines [15], triazines [16], porphyrins [17], and perylenes [18]. These stabilizers share a key feature of poly planar aromatic core that participates in the π -stacking interactions with G-tetrads. Interestingly, the

* Corresponding author.

** Corresponding author at: Institute of Aging Research, School of Medicine, Hangzhou Normal University, Hangzhou, Zhejiang Province 311121, China.

E-mail addresses: zhgwang@aliyun.com (Z. Wang), junping.liu@monash.edu (J.-P. Liu).

end-stacking binding mode of the ligand-like small molecules in G-quadruplex is different from the intercalating binding mode for most duplex DNA–ligand complexes, which is vital to the development of G-quadruplex stabilizers with high specificity. Another important common feature of G-quadruplex stabilizers that aids cellular uptake and improves efficacy is the cation charges located at the central heterocyclic core (RHPS4) or branched substituents (BRACO-19, TMPyP4, TMQP, etc.) [19].

Given extensive studies on G-quadruplex structures and their stabilizers, remarkably few molecules achieved preclinical and clinical phase, none reached the market so far. The major limitations lie in the poor selectivity for the diverse G-quadruplex structures. The intra-molecular telomere G-quadruplex takes the parallel conformation in the K^+ solution under the molecular crowding conditions [20], however many ligands have been developed by targeting anti-parallel and hybrid-type G-quadruplexes [17,18]. Moreover, a number of basic issues that are closely related to the stabilization of G-quadruplex and G-quadruplex–ligand complexes have not been clearly demonstrated at the atomic level. These issues include the conformational alternations of G-quadruplex upon ion bonding and the relationship between the location and quantity of the cation charge in G-quadruplex stabilizers and their binding affinities. To our knowledge, the influences of G-quadruplex central alkali ions on the bound G-quadruplex stabilizers have not been reported.

In the present study, the binding process of potassium ions with human parallel telomeric G-quadruplex was investigated via MD simulation, the conformational changes of G-quadruplex upon K^+ binding were demonstrated and compared with the crystal structure. The interactions between G-quadruplex and two most active stabilizers (RHPS4 and BRACO-19) were systematically analyzed with the central potassium ions under different binding status. The binding affinities of RHPS4 and BRACO-19 evaluated by the binding free energies were in good agreement with the experimental data. Our results demonstrated a correlation between the stabilizer binding strength and the location of G-quadruplex central K^+ , providing fundamental data for a regulated binding between G-quadruplex and ligands in the design and development of G-quadruplex stabilizers.

2. Materials and methods

2.1. Data

The initial structure of human parallel telomeric G-quadruplex was retrieved from PDB data bank with the ID of 1KF1 [21]. The X-ray structure is consisted of $d[AG_3(TTAGGG)_3]$, three potassium ions coordinated in the central channel, and 68 crystal waters. To investigate the binding process of K^+ , models based on the crystal structure and the one with central K^+ removed were generated. As for the studies on the interactions of G-quadruplex with stabilizers, the atomic partial charges of ligands were calculated by the restricted electrostatic potential (RESP) method using Gaussian 03 software [22]. The basis set of HF/6-31G(d) was applied towards the B3LYP/6-31G(d) optimized ligand structures [23,24]. The force field parameters were then generated for each ligand using the Antechamber tool. Four binding complex models for each ligand were generated with the G-quadruplex central channel under the status of zero K^+ , one K^+ at the upper site, one K^+ at the lower site, and 2 K^+ , respectively (Fig. 1a). The crystal waters that superimposed with the bound ligands were removed. Each G-quadruplex–stabilizer complex was immersed into the center of a truncated octahedron box of TIP3P water molecules with a margin distance of 12.0 Å, potassium counterions were added by using the AMBER XLEAP module to keep system in electric neutrality. All

Table 1
MD simulation models.

Model	Stabilizer charge ^a	K^+ ions ^b	Waters ^c	Time scale ^d
1KF1-crystal	–	3 (18)	4856	150
1KF1- K^+ binding	–	0 (21)	4857	150
1KF1-RHPS4	1 × 2	0 (19)	4771	250
1KF1-RHPS4	1 × 2	1 (18)	4765	170
1KF1-RHPS4	1 × 2	1 (18)	4767	100
1KF1-RHPS4	1 × 2	2 (17)	4765	200
1KF1-BRACO-19	3 × 2	0 (15)	4984	140
1KF1-BRACO-19	3 × 2	1 (14)	4972	120
1KF1-BRACO-19	3 × 2	1 (14)	4975	200
1KF1-BRACO-19	3 × 2	2 (13)	4990	200

^a Total net charges of stabilizers equal the charge of single stabilizer multiplied by the number of stabilizers.

^b Number of in-core and environmental (in parentheses) potassium ions.

^c Number of water molecules in MD models.

^d Time scales were in nanosecond.

the MD simulation models and their compositions were listed in Table 1.

2.2. Molecular dynamics simulations

All MD simulations were performed using the AMBER 12 software [25]. FF99SB and parmbsc0 force fields within AMBER12 were applied for G-quadruplex, which have been validated by many nanoseconds state-of-the-art molecular dynamics (MD) simulations [26,27]. Standard Amber ion parameter was used for the environmental K^+ (radius 2.658 Å and well depth 0.00328 kJ mol^{−1}) [28], and the calibrated parameter was used for the K^+ (radius 1.705 Å and well depth 0.1936829 kJ mol^{−1}) that located in the G-tetrad center [29]. Each model was firstly energy minimized by the steepest descent method for 2000 steps with G-quadruplex, central K^+ and stabilizers (if have) restricted by a harmonic constraint of 100 kcal mol^{−1} Å^{−2}, and minimization by the conjugate gradient method was further performed for 5000 steps with no constraint. Then the system was gradually heated from 0 K to 300 K under the NVT ensemble over a period of 200 ps, during which Langevin thermostat with coupling coefficient of 1.0 ps and a weak constraint of 10 kcal mol^{−1} Å^{−2} on nucleotides, central K^+ and stabilizers (if have) were applied. Each model was subsequently subjected to an equilibrium simulation for 200 ps by removing all constraints. Finally, a production simulation for each model was conducted under NPT ensemble. Periodic boundary conditions were applied, system temperature was kept 300 K by Berendsen thermostat method with the time constant of 1 ps, isotropic constant pressure was maintained by Berendsen pressure coupling algorithm with the time constant of 1 ps. Covalent bonds containing hydrogen atoms were constrained by the SHAKE algorithm [30]. The long-range electrostatic interactions were treated by the Particle Mesh Ewald (PME) method [31]. The cutoffs for long-range electrostatic and Van der Waals interactions were both set to 10.0 Å. The time step was set to 2 fs in all simulations, and the coordinates were saved every 1 ps to record the MD trajectory.

2.3. Principal components analysis (PCA)

Also termed as “essential dynamics”, PCA filters the essential degrees of freedom from a number of local fluctuations in MD. The principle of PCA has been described in detail elsewhere [32]. PCA analysis was carried out for the K^+ binding process using the method of Interactive Essential Dynamics (IED) [33]. The PTRAJ module in AMBER12 was applied, and the backbone atoms of G-quadruplex were selected for PCA analysis. Trajectory projections on certain eigenvectors were conducted to determine coupled motions between different eigenvectors. The graphical summary

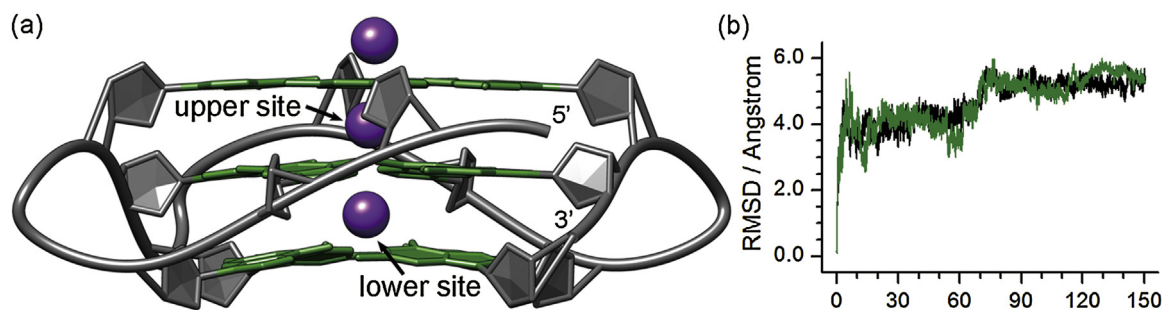


Fig. 1. Structure of the human telomere parallel G-quadruplex and the RMSD fluctuations. (a) For clarity, only G-tetrad composing guanine nucleotides were shown in green. (b) The RMSDs of the crystal and the K⁺ binding models were in black and green, respectively. (For interpretation of the references to color in this figure legend, the reader is referred to the web version of this article.)

of motions along a particular eigenvector was shown in porcupine plot generated by VMD software [34].

2.4. Molecular docking

Molecular docking calculations were performed using the Autodock Vina software [35], which has been reported to be of high accuracy of prediction. The rotatable bonds of all ligands were set flexible, and G-quadruplexes with the central potassium ions under different binding status were set as rigid receptor. Centered at the geometric center of the second G-tetrad, the grid box for docking was set as a $40 \times 40 \times 46 \text{ \AA}^3$ cuboid, which is large enough to include the whole G-quadruplex structure. All the other parameters were set as default.

2.5. Binding free energies

The binding free energies between G-quadruplex and stabilizers were obtained by performing the MM-PBSA (molecular mechanics/Poisson–Boltzmann surface area) calculations [36], and the snapshots of the last 2 ns with an interval of 10 ps were extracted for the calculation. The binding free energy (ΔG_{bind}) was computed from the free energy difference between the binding complex (G_{complex}) and the sum of nucleotides (G_{quad}) and ligands (G_{lig}) as follows:

$$\Delta G_{\text{bind}} = G_{\text{complex}} - (G_{\text{quad}} + G_{\text{lig}}) \quad (1)$$

Each term was estimated as follows:

$$G = E_{\text{MM}} + G_{\text{solv}} - TS \quad (2)$$

where E_{MM} represents the molecular mechanics energy in gas phase, G_{solv} is the solvation free energy, and TS represents the entropy contribution. The E_{MM} term consists of internal strain energy (E_{int}), van der Waals energy (E_{vdW}), and electrostatic energy (E_{ele}):

$$E_{\text{MM}} = E_{\text{int}} + E_{\text{vdW}} + E_{\text{ele}} \quad (3)$$

The solvation free energy was divided into a polar part (G_{PB}) and a nonpolar part (G_{NP}):

$$G_{\text{solv}} = G_{\text{PB sol}} + G_{\text{NP sol}} \quad (4)$$

Therefore, based on above equations, ΔG_{bind} was calculated according to the following equation:

$$\Delta G_{\text{bind}} = \Delta E_{\text{int}} + \Delta E_{\text{vdW}} + \Delta E_{\text{ele}} + \Delta G_{\text{PB, sol}} + \Delta G_{\text{NP, sol}} - T\Delta S \quad (5)$$

In equation 5, the internal strain energy difference (ΔE_{int}) in our system can be neglected. The polar part of solvation $\Delta G_{\text{PB, sol}}$ was calculated by solving the Poisson–Boltzmann (PB) equations with the interior and exterior dielectric constants being set to be 1 and 80, respectively. The nonpolar part of solvation $\Delta G_{\text{NP, sol}}$ was

determined by the solvent accessible surface area (SASA) with the AMBER MOLSURF module, according to the equation:

(6) $\Delta G_{\text{NP, sol}} = \gamma \Delta \text{SASA} + \beta$ where surface tension γ and offset β were set to be $0.0072 \text{ kcal mol}^{-1} \text{ \AA}^2$ and 0, respectively. The entropy term $T\Delta S$ was calculated by performing normal mode analysis with the NMODE [37] module in AMBER 12 under default settings.

3. Results and discussion

3.1. Binding process of K⁺ to G-quadruplex

The root-mean-square deviation (RMSD) profiles of the K⁺ binding and crystal models showed similar fluctuations, especially in the period of 70–150 ns, indicating their comparable stabilities (Fig. 1b). The key conformations corresponding to the K⁺ binding process were retrieved from the MD trajectory of the K⁺ binding model (Fig. 2). The initial binding started at 8.221 ns (Fig. 2a), at which time the 5'-adenine has already flipped over the top G-tetrad, leading to the mismatch of G-tetrads and the formation of a near planar $A_1G_8G_{14}$ triad that capped the top gate of the G-tetrads central channel (Figs. 1a and 2a). Therefore, the bottom gate of the G-tetrad became the only valid pathway for the K⁺ binding. Furthermore, the mismatch caused G_4 and G_{22} protruded deeper into the environment than G_{10} and G_{16} (Fig. 2a), making the pathway gate (the bottom G-tetrad $G_4G_{10}G_{16}G_{22}$) under a half-opened status. When the K⁺ located above G_4 , G_{22} , G_{10} and below G_{16} at 8.250 ns, the top coordinated water of the binding K⁺ traversed into the G-tetrads center completely (Fig. 2b). The K⁺ was in a trapped status for over 2.2 ns till it was repulsed through the G-tetrad gate by a second environmental K⁺ (Fig. 2c–e). The binding K⁺ finally located at the lower binding site at 10.895 ns, all the G-tetrads recovered to the coplanar form, but the 5'-adenine remained the flipped conformation (Fig. 2f).

The K⁺ binding process in parallel telomere G-quadruplex was similar to that in the hybrid-I and two-layered basket type G-quadruplexes [38,39], suggesting an inherent property of G-tetrad structures. The conformational flip of 5'-adenine resulted in additional π - π interactions with G_{20} (Fig. 2f) and could probably reduce the solvation free energy of G-quadruplex. Similar conformational changes were discovered in the crystal model as well (Fig. S1). Thus, besides the function in determining the K⁺ binding pathway, the 5'-adenine may also play a key role in the stabilization of G-quadruplex structure.

3.2. Conformational alternations of G-quadruplex

The distance between the bound K⁺ and the geometric center of the four O6 atoms of the central G-tetrad $G_3G_9G_{15}G_{21}$ (CCG) can be recognized as a marker of the K⁺ binding process. Before the distance converged to $\sim 1.12 \text{ \AA}$, a sudden decrease (Fig. 3a) and the

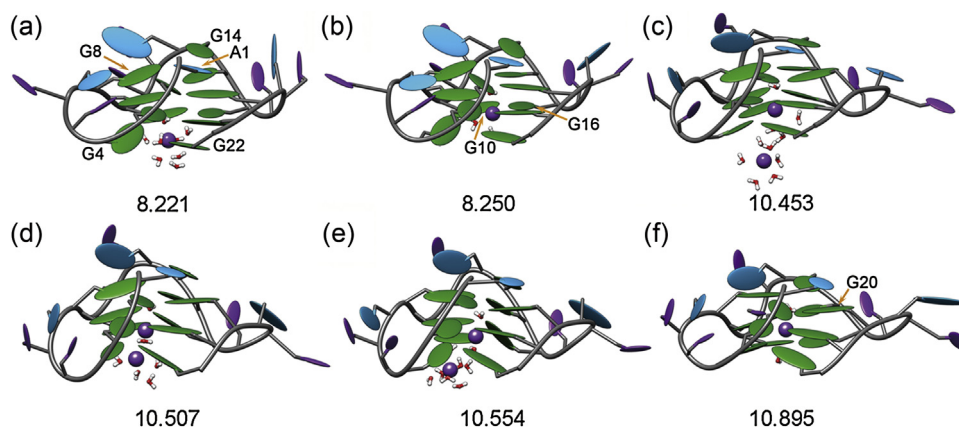


Fig. 2. Binding process of K^+ with human telomere parallel G-quadruplex. The bases of adenine, thymine and guanine nucleotides were colored cyan, purple and green, respectively. K^+ ions were shown as purple spheres, waters were displayed as ball-and-stick models. (For interpretation of the references to color in this figure legend, the reader is referred to the web version of this article.)

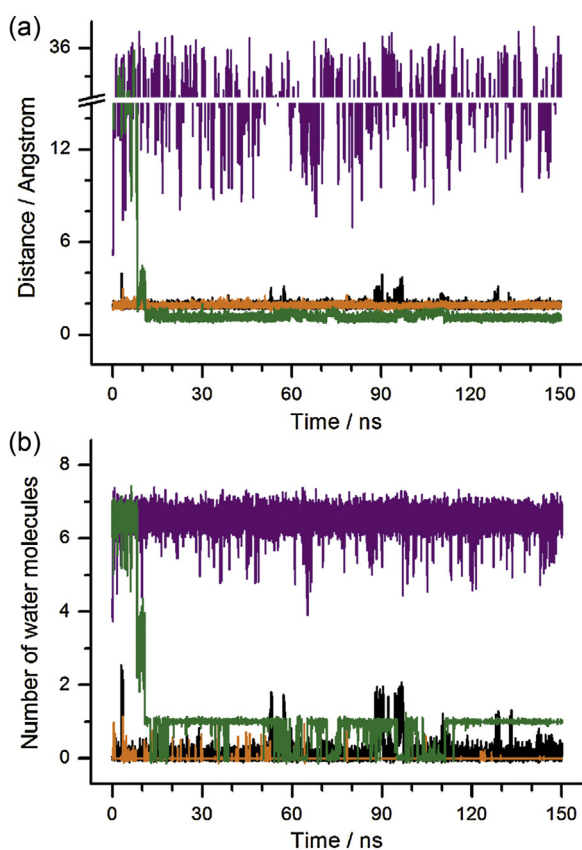


Fig. 3. The variations of distances between the bound K^+ and CCG (a) and the coordinated waters around K^+ (b). Fluctuations related to the bound K^+ in the K^+ binding model were colored green. For that in the crystal model, purple for the top located K^+ , orange for the upper site coordinated K^+ and black for the lower site coordinated K^+ were set. (For interpretation of the references to color in this figure legend, the reader is referred to the web version of this article.)

subsequent fluctuations were observed, the points of time when these changes occurred were in consistent with the K^+ binding process (Fig. 2). Since the ability of alkali metal ions in stabilizing G-quadruplex is related to their free energies of hydration [40], the hydration status of the bound K^+ was monitored by defining the waters within 3.5 Å of K^+ as coordinated molecules. The coordinated waters of the binding K^+ quickly decreased from 6–7 to 2–4 and finally became 1 for most of the MD simulation, the changing times agreed with the binding process and the distance changes

(Fig. 3b and a). Notably, in the crystal model the K^+ located above the top G-tetrad leaked into environment quickly, suggesting its weak binding affinity with G-quadruplex. The K^+ ions coordinated at the upper and lower sites were stable, and their distances towards CCG were both ~ 1.95 Å, indicating that the two K^+ ions located symmetrically across the plane of central G-tetrad. The difference in the distances of the central K^+ to CCG between the K^+ binding and crystal models suggested that the single bound K^+ was more close to the G-tetrads center, making it more feasible to neutralize the electronegative charges from the O6 atoms of all G-tetrads.

The RMSF profiles of the K^+ binding and crystal models indicated that the three double-chain-reversal loops ($T_5T_6A_7$, $T_{11}T_{12}A_{13}$ and $T_{17}T_{18}A_{19}$) contributed most flexibilities of the G-quadruplexes (Fig. 4a). In PCA analysis, the eigenvalues of the first 30 eigenvectors for both ensembles were shown in Fig. 4b. Over 76.1% and 68.8% fluctuations were due to the concerted motions specified by the first six eigenvectors and 33.7% and 35.6% by the first eigenvectors in the K^+ binding and the crystal models, respectively. The two-dimensional projections defined by the first two eigenvectors assembled in some certain regions, indicating a concerted conformational alternation of the two ensembles (Fig. S2). The porcupine plots revealed that in the crystal model, the dominant motions along the first eigenvector were the upward movement of the 5'-termini and the $T_{17}T_{18}A_{19}$ loop (Fig. 4c). There were similar motions along the second eigenvector for the 5'-termini and $T_{11}T_{12}A_{13}$ loop (Fig. 4d). Except for the promoted downward motions of G_{21} and G_{22} , the first eigenvector in the K^+ binding model represented similar motions as that in the crystal model (Fig. 4e and c), and the second eigenvector mainly stood for the upward motions of the 5'-termini and the $T_{17}T_{18}A_{19}$ loop (Fig. 4f).

3.3. Stabilizer binding modes with G-quadruplex under different status of central K^+

The molecules of RHPS4 [41] and BRACO-19 [42] that show high stabilization abilities towards G-quadruplexes were retrieved from the solution NMR and X-ray diffraction determined G-quadruplex-ligand structures (PDB ID: 1NZM and 3CE5). The K^+ located above the top G-tetrad was removed in docking calculations since it quickly escaped into environment. For both stabilizers, Autodock Vina predicted well-superimposed binding conformations with their PDB structures (Fig. S3), validating our docking calculation method.

The structures of the predicted G-quadruplex-stabilizer complexes were shown in Fig. 5. The two stabilizers were predicted to bind with the telomere parallel G-quadruplex with the same

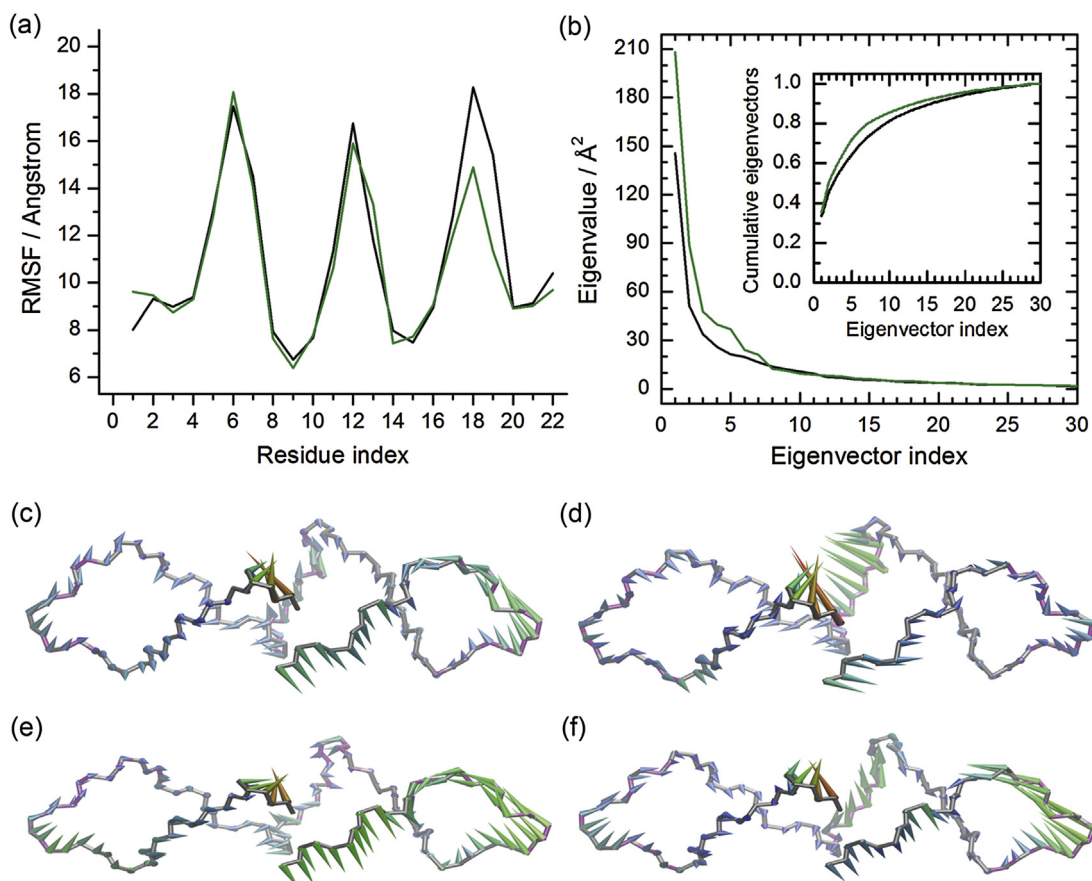


Fig. 4. RMSF and principal component analysis. (a) RMSF were shown as black and green lines for the crystal and the K⁺ binding models, respectively. (b) Eigenvalue profiles constructed by the first 30 eigenvectors from PCA analysis of the crystal and the K⁺ binding MD ensembles, which were represented by black and green lines, respectively. (c) and (d) represented the dominant motions along the first and the second eigenvectors in the crystal ensemble by porcupine plot, respectively. (e) and (f) represented the corresponding motions in the K⁺ binding ensemble. All the loop backbones in the porcupine plot were colored purple. (For interpretation of the references to color in this figure legend, the reader is referred to the web version of this article.)

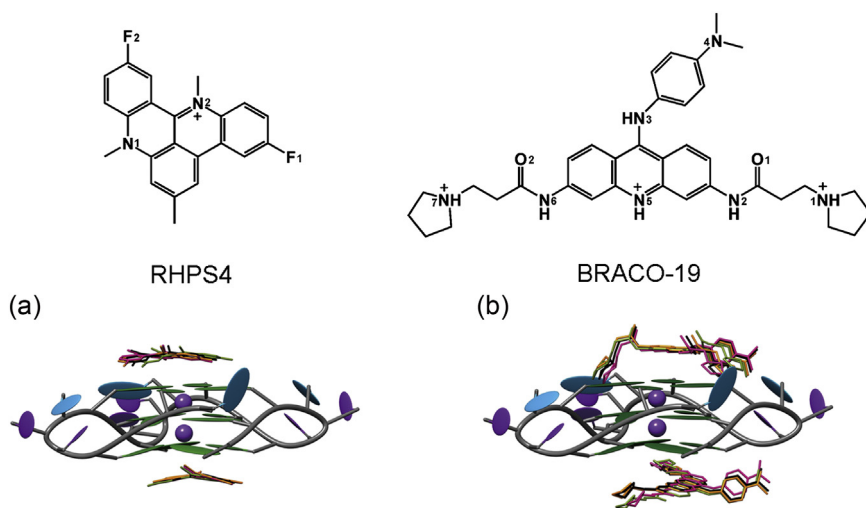


Fig. 5. Stabilizer structures and the corresponding binding conformations with G-quadruplex. With the G-quadruplex under the zero K⁺, 1 K⁺ (upper site), 1 K⁺ (lower site) and 2 K⁺ bound status, the corresponding conformations for the bound stabilizers were colored black, pink, orange and green, respectively. For clarity, both K⁺ were displayed. (For interpretation of the references to color in this figure legend, the reader is referred to the web version of this article.)

molecular proportion of 2:1. Both RHPS4 and BRACO-19 bound with the G-quadruplex through stacking on both the top and bottom G-tetrads (Fig. 5a and b). The docked conformations of RHPS4 were pretty close to that in the NMR structure of 1NZM (Fig. S3a). The branched groups of the top bound BRACO-19 bent towards

the nearby grooves, while in the bottom stacked BRACO-19 such feature was hardly to find but instead the whole molecule tended to stack on the bottom G-tetrad in a planar form (Fig. 5b). With G-quadruplex under different binding status of central K⁺, similar binding conformations for both RHPS4 and BRACO-19 were

obtained (Fig. 5a and b). Therefore, the status of central K^+ showed no apparent impact on the docking conformations of stabilizers, indicating that the π - π interactions between the cyclic part of the stabilizers and G-tetrads is probably the main factor in determining the stabilizer binding conformations.

3.4. Structural variations of the binding complexes

MD simulations on the eight G-quadruplex-stabilizer models were performed to investigate their conformational variations and binding stabilities. Under the status of no central K^+ bound in G-tetrads, the RMSDs of the RHPS4 and BRACO-19 bound G-quadruplexes were about 5.0 and 5.7 Å (Fig. 6a and e), respectively. And when there was 1 K^+ at the upper binding site or 1 K^+ at the lower binding site or 1 K^+ each at both sites, the RMSD values were about 4.5, 4.6 and 3.9 for the RHPS4 bound G-quadruplexes (Fig. 6b–d) and 4.5, 4.3, and 4.3 for the BRACO-19 bound ones (Fig. 6f–h), respectively. The RMSD differences between the no central K^+ and the one or two central K^+ bound G-quadruplexes indicated that the introduction of K^+ into the G-tetrads could decrease the extents of the structural variations of G-quadruplexes and is thus good for their stabilities. The RMSD values of the bound stabilizers were calculated as well. All the top and bottom stacked RHPS4 molecules showed close RMSDs, and the value of ~ 0.7 Å indicated that the bindings between RHPS4 and G-quadruplexes were of high stability (Fig. 6a–d). Probably because of the molecular flexibility, BRACO-19 showed increased RMSD values. Except for the no central K^+ bound G-quadruplex-BRACO-19 model in which the top and bottom bound BRACO-19 showed different RMSDs (3.3 and 2.5 Å, respectively) (Fig. 6e), both of the top and bottom stacked BRACO-19 molecules showed similar RMSD values in the 1 K^+ upper site (3.0 Å), 1 K^+ lower site (2.8 Å) and 2 K^+ (2.6 Å) bound G-quadruplex-BRACO-19 models (Fig. 6f–h). The profiles of BRACO-19 RMSD curves indicated their stable bindings with the parallel G-quadruplexes.

It is notable that, except for the no central K^+ bound G-quadruplex-BRACO-19 model (Fig. 6e), all the other stabilizer bound G-quadruplexes showed decreased RMSD values compared to the crystal model (~ 5.2 Å, Fig. 1b), indicating the stabilizing effects of RHPS4 and BRACO-19 towards the G-quadruplex structures. The RMSFs of the stabilizer bound G-quadruplexes were calculated to investigate the structural fluctuations during the whole MD simulations (Fig. S4). The RMSF values of the G3 (10.2 Å) and G4 (11.4 Å) in the no central K^+ bound G-quadruplex-RHPS4 model and the G3 (12.4 Å), G4 (14.1 Å), G20 (10.6 Å) and G21 (10.0 Å) in the no central K^+ bound G-quadruplex-BRACO-19 model were extraordinary high (Fig. S4), indicating the large conformational fluctuations of the corresponding guanine nucleotides. All the other stabilizer bound G-quadruplexes showed pretty similar RMSF profiles to that of the crystal model (Figs. S4 and 4a), implying that these G-quadruplexes showed comparable extents of structural fluctuations.

The averaged structures of the binding complexes based on the last 2 ns MD trajectories were obtained and compared with the crystal structure. As demonstrated in Fig. 7, all the top and bottom bound stabilizers were in close contact with the G-quadruplexes. Compared to the initial binding conformations (Fig. 5), some planar rotations for RHPS4 and side chain oscillations for BRACO-19 can be found (Fig. 7). However, these changes did not break up the bindings of G-quadruplex and stabilizers, because there were still good π -stacking interactions between the backbones of stabilizers and the G-quadruplex guanines (Fig. 7). In agreement with the RMSD analysis (Fig. 6a and e), G-quadruplexes in the no central K^+ bound models showed great conformational variations (Fig. 7a and e). Like the process in the K^+ binding model, one environmental K^+ entered into the central channel of G-tetrads through the bottom

Table 2

Average occupancy (%) of eight Hoogsteen hydrogen bonds in each G-tetrad along the entire MD trajectories.

G-tetrads	Stabilizers	Binding state of central K^+ ^a			
		0 K^+	1 K^+ upper	1 K^+ lower	2 K^+
top G-tetrad	RHPS4	15.34	99.73	82.71	98.91
	BRACO-19	68.97	99.03	86.00	99.41
central G-tetrad	RHPS4	11.81	96.38	94.18	97.79
	BRACO-19	34.45	99.09	97.02	97.82
bottom G-tetrad	RHPS4	15.55	78.68	99.31	99.11
	BRACO-19	37.79	59.42	99.51	99.21

^a The subscripted words indicated that the K^+ coordinated at the upper and lower binding sites, respectively.

pathway in the model of G-quadruplex-0 K^+ – RHPS4 (Figs. 7a and S5). But in this model the G-tetrads cannot completely recover to the original crystal form, because two new G-tetrads ($G_3G_8G_{14}G_{20}$ and $G_4G_9G_{15}G_{21}$) and one G-triad ($G_{10}G_{16}G_{22}$) structures formed, in which the guanine bases interacted through hydrogen bonds. Following to the stretch and flip of the 5'-adenine, G_2 located above the plane of the $G_3G_8G_{14}G_{20}$ G-tetrad. And the K^+ finally located between the planes of the two new G-tetrads (Fig. 7a). In the model of Fig. 7e, no K^+ can enter into the G-tetrads center since both the top and the bottom gates of the G-tetrads were fully covered by the BRACO-19. And the binding of BRACO-19 caused the formation of one flanking strand (the last strand) and a three-layered triplex, a structure that is pretty similar to the folding intermediate of human G-quadruplex [43]. The reason that RHPS4 and BRACO-19 showed different effects towards G-quadruplexes is probably caused by their apparent distinctions in the structural characteristics and molecular dimensions. All the other G-quadruplexes in Fig. 6b–d and f–h showed good superimpositions with the crystal model in their G-tetrads, and most conformational variations occurred at the loop regions, which is agreed with the RMSF analysis (Fig. S4). It should be noted that in all models the 5'-adenine showed similar flipped conformations (Figs. 7 and S1), indicating the conformational characteristics of this terminal nucleotide.

3.5. Hydrogen bonding

Hoogsteen hydrogen bonds ($N2-H \cdots N7$ and $N1-H \cdots O6$) are the main contributing force in the G-tetrad layer, the status of which should be the prime marker of the stability of G-quadruplex. With the criteria of the bond length < 3.5 Å and the bond angle $> 120^\circ$, hydrogen bond information was analyzed for all the MD ensembles. The hydrogen bond occupancy (HBO) in each G-tetrad were calculated along the MD trajectories (Fig. 8), and the average occupancies of the eight Hoogsteen hydrogen bonds in each G-tetrad were listed as well (Table 2). Consistent with the conformational analysis (Fig. 7a and e), almost all the Hoogsteen hydrogen bonds were seriously damaged in the models that had no K^+ in the G-tetrads centers (Fig. 8a and e, Table 2). In the models that had one K^+ located at the upper binding site, the Hoogsteen hydrogen bonds in the top and the central G-tetrads were of high occupancies, while the HBO in the bottom G-tetrad showed decreased values (Fig. 8b and f, Table 2). In the models that had one K^+ located at the lower binding site, the central and the bottom G-tetrads showed high HBOs and the top G-tetrad showed decreased HBO (Fig. 8c and g, Table 2). It should be noted that in the HBO decreased G-tetrads, all the $N1-H \cdots O6$ hydrogen bonds showed relatively higher occupancies than $N2-H \cdots N7$ (Fig. 8b, c, f and g), which may be caused by the central K^+ that had strong electrostatic attractions to the guanine O6 atoms and kept the O6 atom in a proper distance from the polar hydrogen of N1. For the models that had two central K^+ ions, the Hoogsteen hydrogen bonds were of high occupancies in all of the three G-tetrads (Fig. 8d and h, Table 2), indicating the high sta-

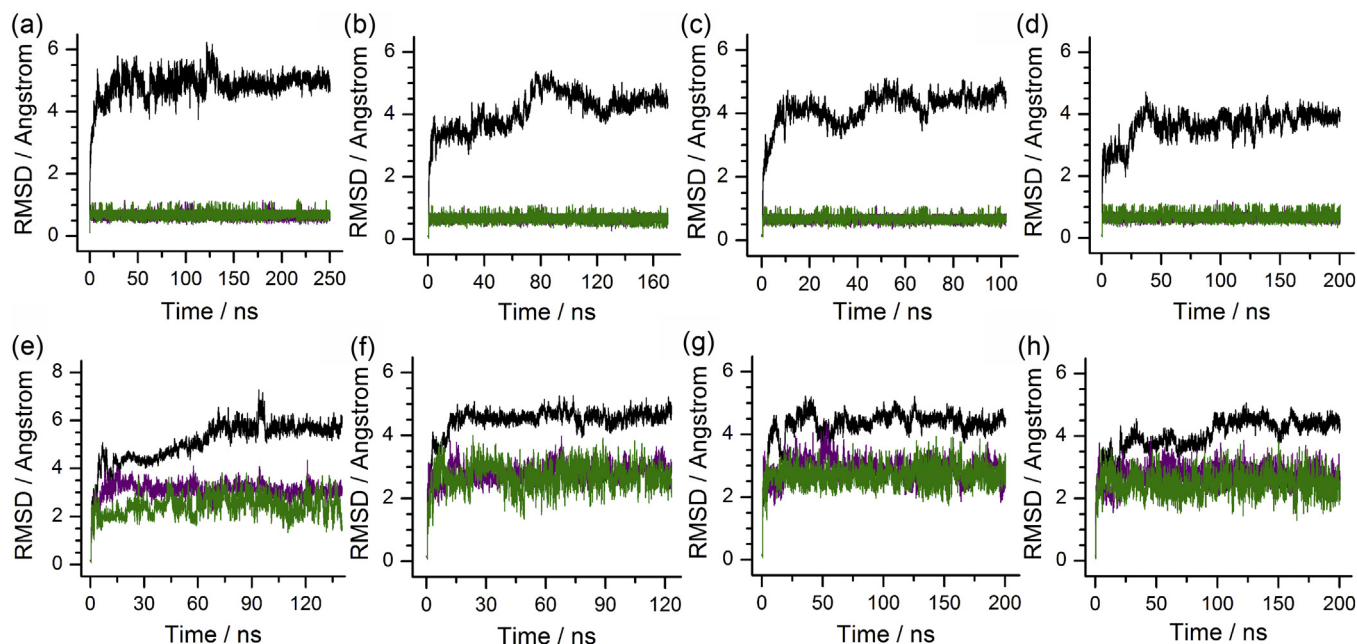


Fig. 6. RMSDs of the stabilizer bound G-quadruplexes. The black curves in (a)–(d) and (e)–(h) corresponded to the RMSD profiles of the RHPs4 and BRACO-19 bound G-quadruplexes with the G-tetrads under the zero K^+ , 1 K^+ (upper site), 1 K^+ (lower site) and 2 K^+ bound status, respectively. The RMSDs of the top and bottom stacked stabilizers were shown as purple and green lines, respectively. (For interpretation of the references to color in this figure legend, the reader is referred to the web version of this article.)

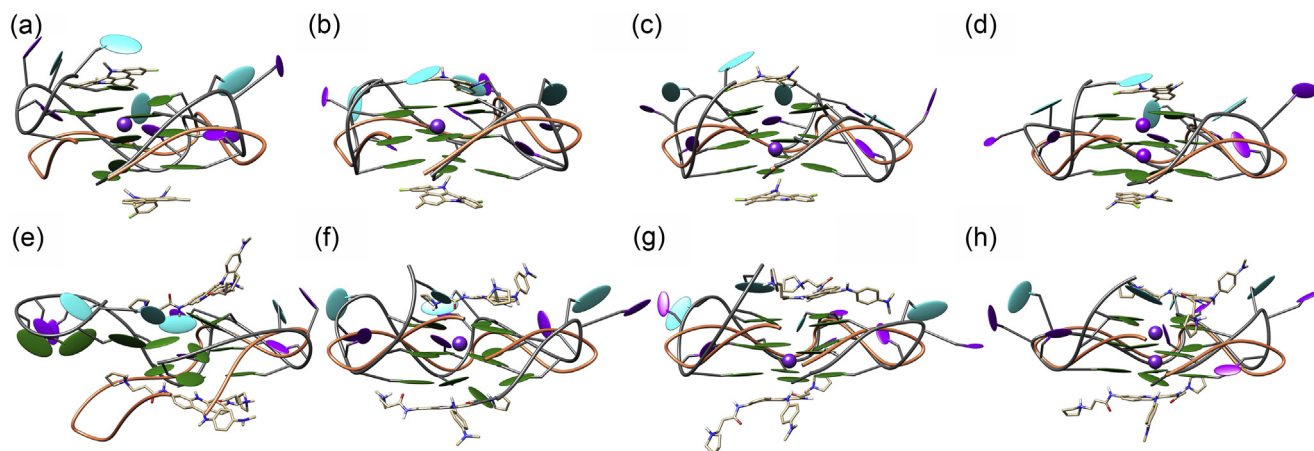


Fig. 7. Averaged structures of the G-quadruplexes (dim grey) from the last 2 ns MD trajectories superimposed with the crystal structure (orange). RHPs4 in (a)–(d) and BRACO-19 in (e)–(h) were shown in stick, the central K^+ were shown as purple spheres. (For interpretation of the references to color in this figure legend, the reader is referred to the web version of this article.)

bilities of the corresponding G-quadruplexes. And the $N2-H \cdots N7$ showed higher occupancies than the $N1-H \cdots O6$ hydrogen bonds (Fig. 8d and h), this was probably caused by the fact that the strength of repulsion between the two K^+ cations was superior to that of the electrostatic attractions between K^+ and guanine O6 atoms.

The HBOs of the crystal and the K^+ binding models were calculated as well (Fig. S6). The average HBOs of the G-tetrads in the crystal and the K^+ binding models were comparable to that in the stabilizers bound G-quadruplex-2 K^+ (Fig. 8d and h) and G-quadruplex-1 K^+_{lower} models (Fig. 8c and g), respectively. The molecular Hoogsteen hydrogen bonds occupancies were further calculated. The molecular HBOs of the crystal and the K^+ binding G-quadruplexes were 98.18% and 90.91%, respectively. And the corresponding molecular HBOs of the stabilizers bound G-quadruplexes were 98.60% in the G-quadruplex-2 K^+ -2 RHPs4 model, 98.91% in the G-quadruplex-2 K^+ -2 BRACO-19 model and 92.07% in the G-quadruplex-1 K^+_{lower} -2 RHPs4 model, 94.18% in

the G-quadruplex-1 K^+_{lower} -2 BRACO-19 model, respectively. The values of the molecular based HBOs indicated that both RHPs4 and BRACO-19 could improve the stability of the G-tetrads core, which is good for the overall G-quadruplex structure.

Hydrogen bonding is an important contributing component in most macromolecule–ligand interactions. Systematic search for hydrogen bonds between G-quadruplex and stabilizers were performed (Table 3). Probably because of the rigid framework and the lack of polar hydrogens in RHPs4, no intermolecular hydrogen bonds were found in the binding complexes of G-quadruplex-RHPs4. However, several intermolecular hydrogen bonds were found in each G-quadruplex-BRACO-19 complex (Table 3), this may be one reason that BRACO-19 showed stronger stabilization effect towards the G-tetrads compared to RHPs4. Interestingly, only the top stacked BRACO-19 formed hydrogen bonds with G-quadruplex in the model that has one K^+ located at the upper binding site, and vice versa for the model that has one K^+ located

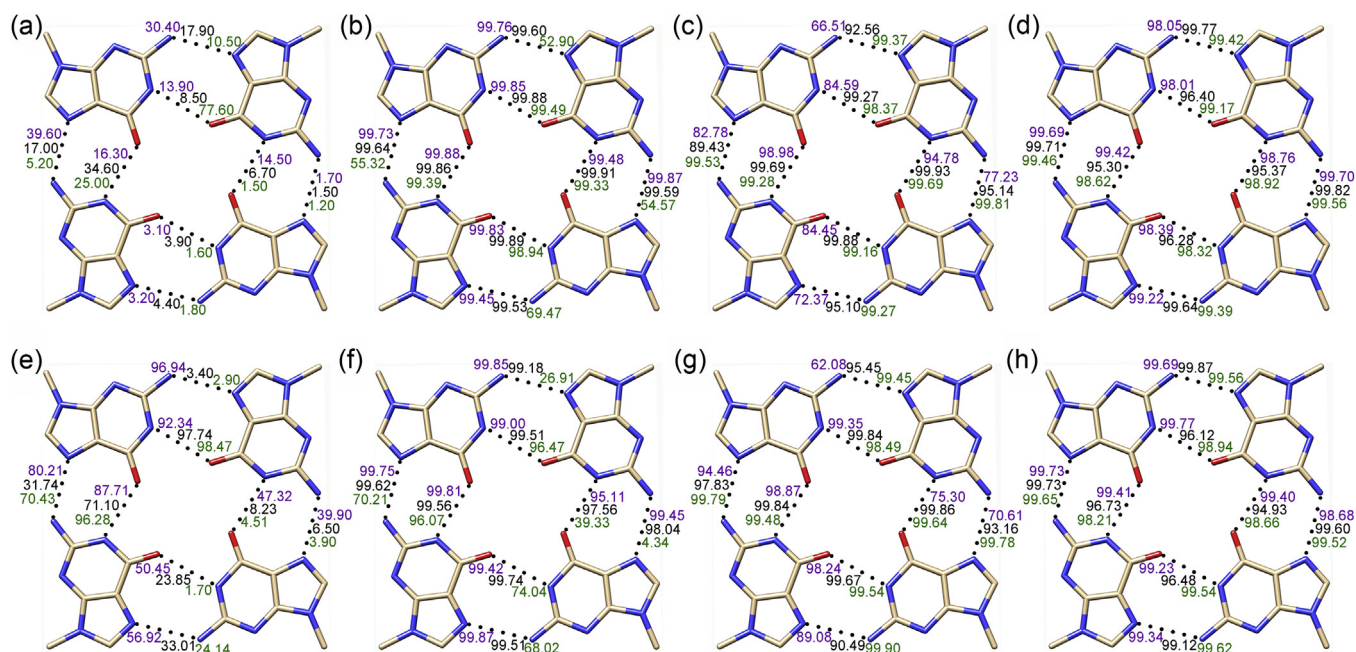


Fig. 8. Hoogsteen hydrogen bond occupancy analysis of the stabilizer bound G-quadruplexes. Occupancy was provided as a percentage of the MD simulation time. (a)–(d) and (e)–(h) represented the RHPS4 and BRACO-19 bound models with the G-tetrads under the zero K⁺, 1 K⁺ (upper site), 1 K⁺ (lower site) and 2 K⁺ bound status, respectively. The occupancies of hydrogen bonds in the top, central and bottom G-tetrads were in purple, black and green colored numbers, respectively. (For interpretation of the references to color in this figure legend, the reader is referred to the web version of this article.)

Table 3
Hydrogen bonds between BRACO-19 and G-quadruplex.

Model ^a	Donor	Acceptor ^b	Occupancy ^c	Distance ^d	Angle ^e
0 K ⁺	G8@O1P	A23@H7 A23@N7	64.57	2.87	25.47
	G20@O1P	A23@H1 A23@N1	35.94	2.91	31.37
	G10@O6	U24@H5 U24@N5	35.68	2.92	21.79
	T11@O2P	U24@H1 U24@N1	35.40	2.86	27.77
	G20@O5'	A23@H1 A23@N1	35.10	3.07	35.37
1 K ⁺ upper	G14@O4'	A23@H3 A23@N3	30.66	2.97	34.29
	G14@O1P	A23@H6 A23@N6	71.03	2.98	19.84
	G20@O4'	A23@H2 A23@N2	50.24	3.09	39.87
	G20@O5'	A23@H2 A23@N2	41.59	3.19	23.20
1 K ⁺ lower	G22@O6	U24@H3 U24@N3	63.79	3.04	24.04
	T11@O2P	U24@H1 U24@N1	57.95	2.84	26.62
	T5@O2P	U24@H7 U24@N7	40.20	2.88	27.72
	G20@O4'	A23@H2 A23@N2	57.56	3.02	39.91
2 K ⁺	G20@O5'	A23@H2 A23@N2	54.19	3.13	28.45
	T5@O2P	U24@H7 U24@N7	45.21	2.88	24.90
	T11@O2P	U24@H1 U24@N1	41.40	2.85	26.59

^a The binding models of 1KF1 and BRACO-19 were listed according to the bound status of G-quadruplex central K⁺ ions, with the subscripted words indicating their respective coordinations.

^b A23 and U24 indicated the BRACO-19 molecules that stacked above the top G-tetrad and under the bottom G-tetrad, respectively.

^c The hydrogen bonds with the occupancy of whole MD simulation time over 30% were listed.

^d Time averaged hydrogen bond length in angstrom.

^e Time averaged hydrogen bond angle in degree.

at the lower binding site (Table 3), indicating the impact of the central K⁺ on the stabilizer binding. In the model that has 2 K⁺ in the G-tetrads center, each of the top and bottom stacked BRACO-19 formed two hydrogen bonds with G-quadruplex. And in the model that has no central K⁺ the top and bottom bound BRACO-19 respectively formed four and two intermolecular hydrogen bonds with G-quadruplex (Table 3). Notably, most of the intermolecular hydrogen bonds formed between the sidechain polar hydrogens of BRACO-19 and the oxygen atoms of the sugar and phosphate groups of the nucleotides that have exposed guanine or adenine bases, occasionally the central polar hydrogens of BRACO-19 can form hydrogen bonds with the guanine O6 atoms as well (Table 3). The information of the intermolecular hydrogen bonding may be useful for the structural optimization of G-quadruplex stabilizers.

3.6. Binding free energies

Quantitative evaluation of the binding affinities of the two stabilizers with G-quadruplex were performed using the MM-PBSA method. The results indicated that the electrostatic energy (E_{ele}), the van der Waals energy (E_{vdW}) and the nonpolar solvation energy ($E_{\text{np, sol}}$) contributed the main driving forces for the binding of stabilizers (Table 4). However, the polar solvation energy ($\Delta G_{\text{PB, sol}}$) and the entropy component ($T\Delta S$) made unfavorable contributions to the binding (Table 4). According to the equation $\Delta G \approx RT \ln C_{50}$ [24] and the TRAP inhibition values of RHPS4 and BRAOCO-19 [44,45], the experimental binding free energies of RHPS4 and BRAOCO-19 towards G-quadruplex were -8.90 and -9.67 kcal mol⁻¹, respectively. In all models the predicted binding free energies ranged

Table 4
Binding free energies of the G-quadruplex–stabilizer complexes.

G-quad ^a	Stabilizer ^b	Energy component ^c					
		ΔE_{ele}	ΔE_{vdw}	$\Delta G_{\text{PB},\text{sol}}$	$\Delta G_{\text{np},\text{sol}}$	$T\Delta S$	ΔG_{bind}
0 K ⁺	RHPS4 _{upper}	−542.42	−48.35	562.75	−4.84	−20.41	−12.45
	RHPS4 _{lower}	−474.50	−29.88	485.31	−3.25	−16.38	−5.94
1 K ⁺ _{upper}	RHPS4 _{upper}	−480.39	−41.95	492.45	−4.43	−17.15	−17.17
	RHPS4 _{lower}	−432.89	−32.97	437.28	−3.26	−17.18	−14.66
1 K ⁺ _{lower}	RHPS4 _{upper}	−465.29	−38.05	476.48	−4.14	−17.49	−13.51
	RHPS4 _{lower}	−434.16	−31.71	438.13	−3.35	−16.06	−15.03
2 K ⁺	RHPS4 _{upper}	−426.66	−36.87	434.07	−3.86	−17.80	−15.52
	RHPS4 _{lower}	−411.50	−32.11	416.80	−3.31	−16.10	−14.02
0 K ⁺	BRACO-19 _{upper}	−1476.41	−51.74	1478.94	−6.23	−28.75	−26.69
	BRACO-19 _{lower}	−1363.52	−40.42	1365.69	−4.66	−25.11	−17.80
1 K ⁺ _{upper}	BRACO-19 _{upper}	−1480.06	−60.69	1492.13	−6.98	−34.10	−21.50
	BRACO-19 _{lower}	−1337.23	−40.94	1339.50	−4.76	−24.94	−18.49
1 K ⁺ _{lower}	BRACO-19 _{upper}	−1453.20	−59.93	1466.47	−7.00	−30.53	−23.13
	BRACO-19 _{lower}	−1351.81	−44.68	1350.03	−4.89	−25.15	−26.20
2 K ⁺	BRACO-19 _{upper}	−1336.03	−59.64	1344.39	−6.50	−31.05	−26.73
	BRACO-19 _{lower}	−1247.53	−41.47	1250.86	−4.65	−23.18	−19.61

^a The subscripted words of upper and lower indicated the corresponding locations of bound potassium ions within the G-tetrads core.

^b The subscripted words indicated the binding positions of stabilizers, with upper for the binding above top G-tetrad and lower for the binding below bottom G-tetrad, respectively.

^c Energies were in kcal mol^{−1}.

from −5.94 to −17.17 kcal mol^{−1} for RHPS4 and from −17.80 to 26.73 kcal mol^{−1} for BRACO-19 (Table 4). Agreed with the experimental results, our predicted binding affinities of the two stabilizers followed the order of BRACO-19 > RHPS4 (Table 4). The calculated energies could be overestimated, this was probably due to the limitation of the MM-PBSA for highly charged species [46].

The binding free energies of the stabilizers in the no central K⁺ bound models only stood for their affinities towards G-quadruplex under special circumstances, since the G-tetrads were mismatched (Fig. 7a) or under partly corrupted status (Fig. 7e). In the one central K⁺ bound models, the binding affinities of RHPS4 and BRACO-19 were apparently affected by the location of central K⁺, i.e. the top stacked stabilizers showed better binding strength with G-quadruplex when the K⁺ located at the upper binding site, while the bottom stacked stabilizers became advantaged when the K⁺ located at the bottom binding site (Table 4). Probably because of the additional interactions with the flipped 5'-adenine (Fig. 7d and h), the top stacking conformation were the preferred binding mode for both stabilizers in the two central K⁺ bound models. Compared to RHPS4, all the BRACO-19 showed greater binding affinities towards G-quadruplex (Table 4). This is probably because that the intermolecular hydrogen bonds between BRACO-19 and G-quadruplex make the electrostatic interactions more effective and the widely spreading polarities in the sidechains and mainframe of BRACO-19 could lead to stronger van der Waals interactions with G-quadruplex.

4. Conclusions

In this study, the binding process of K⁺ with human telomere parallel G-quadruplex was revealed to be a water-mediated step-wise process through the bottom pathway, since the top gate of G-quadruplex central channel was capped by the flipped 5'-adenine. The conformational fluctuations occurred mainly at the 5'-termini and the double-chain-reversal loop regions in both of the K⁺ binding and the crystal models. The binding status of the central K⁺ showed little effects on the orientations of bound stabilizers. However, the central K⁺ exerted apparent impacts on the binding strength of RHPS4 and BRACO-19, especially in the one central K⁺ bound models. Furthermore, the models with no central K⁺ became mismatched or partly corrupted in their G-tetrad cores, indicating the stabilizers alone cannot stabilize the G-quadruplex structure. The difference in binding affinities between RHPS4 and

BRACO-19 is probably related to the ability to form intramolecular hydrogen bonds and favorable van der Waals interactions with G-quadruplex. The data demonstrated some novel characteristics on the binding of central K⁺ and stabilizers with G-quadruplex, which is useful in G-quadruplex targeted drug design.

Acknowledgement

This work was supported by the National Basic Research Program of China (973 project) (Grant Nos. 2012CB911204, 2012CB911200).

Appendix A. Supplementary data

Supplementary data associated with this article can be found, in the online version, at <http://dx.doi.org/10.1016/j.jmgm.2017.01.006>.

References

- [1] F.W. Smith, Quadruplex structure of Oxytricha telomeric DNA oligonucleotides, *Nature* 356 (6365) (1992) 164–168.
- [2] Y. Wang, D.J. Patel, Guanine residues in d(T₂AG₃) and d(T₂G₄) form parallel-stranded potassium cation stabilized G-quadruplexes with anti glycosidic torsion angles in solution, *Biochemistry-US* 31 (35) (1992) 8112–8119.
- [3] M.P. Horvath, S.C. Schultz, DNA G-quartets in a 1.86 Å resolution structure of an Oxytricha nova telomeric protein-DNA complex, *J. Mol. Biol.* 310 (2) (2001) 367–377.
- [4] A. Siddiqui-Jain, C.L. Grand, D.J. Bearss, L.H. Hurley, Direct evidence for a G-quadruplex in a promoter region and its targeting with a small molecule to repress c-MYC transcription, *Proc. Natl. Acad. Sci. U. S. A.* 99 (18) (2002) 11593–11598.
- [5] A.T. Phan, V. Kuryavyi, S. Burge, S. Neidle, D.J. Patel, Structure of an unprecedented G-quadruplex scaffold in the human c-kit promoter, *J. Am. Chem. Soc.* 129 (14) (2007) 4386–4392.
- [6] J. Dai, D. Chen, R.A. Jones, L.H. Hurley, D. Yang, NMR solution structure of the major G-quadruplex structure formed in the human BCL2 promoter region, *Nucleic Acids Res.* 34 (18) (2006) 5133–5144.
- [7] M.I. Onyshchenko, T.I. Gaynutdinov, E.A. Englund, D.H. Appella, R.D. Neumann, I.G. Panyutin, Stabilization of G-quadruplex in the BCL2 promoter region in double-stranded DNA by invading short PNAs, *Nucleic Acids Res.* 37 (22) (2009) 7570–7580.
- [8] S. Kumari, A. Bugaut, J.L. Huppert, S. Balasubramanian, An RNA G-quadruplex in the 5' UTR of the NRAS proto-oncogene modulates translation, *Nat. Chem. Biol.* 3 (4) (2007) 218–221.
- [9] A. Bugaut, R. Rodriguez, S. Kumari, S.-T.D. Hsu, S. Balasubramanian, Small molecule-mediated inhibition of translation by targeting a native RNA G-quadruplex, *Org. Biomol. Chem.* 8 (12) (2010) 2771–2776.

- [10] M.L. Bochman, K. Paeschke, V.A. Zakian, DNA secondary structures: stability and function of G-quadruplex structures, *Nat. Rev. Genet.* 13 (11) (2012) 770–780.
- [11] W.E. Wright, V.M. Tesmer, K.E. Huffman, S.D. Levene, J.W. Shay, Normal human chromosomes have long G-rich telomeric overhangs at one end, *Gene Dev.* 11 (21) (1997) 2801–2809.
- [12] H. Han, L.H. Hurley, G-quadruplex DNA: a potential target for anti-cancer drug design, *Trends Pharmacol. Sci.* 21 (4) (2000) 136–142.
- [13] S. Neidle, The current status of telomeric G-quadruplexes as therapeutic targets in human cancer, *FEBS J.* 277 (5) (2010) 1118–1125.
- [14] A.T. Phan, Human telomeric G-quadruplex: structures of DNA and RNA sequences, *FEBS J.* 277 (5) (2010) 1107–1117.
- [15] R.J. Harrison, S.M. Gowan, L.R. Kelland, S. Neidle, Human telomerase inhibition by substituted acridine derivatives, *Bioorg. Med. Chem. Lett.* 9 (17) (1999) 2463–2468.
- [16] J. Riou, L. Guittat, P. Mailliet, A. Laoui, E. Renou, O. Petitgenet, F. Megnin-Chanet, C. Helene, J. Mergny, Cell senescence and telomere shortening induced by a new series of specific G-quadruplex DNA ligands, *Proc. Natl. Acad. Sci. U. S. A.* 99 (5) (2002) 2672–2677.
- [17] H. Han, D.R. Langley, A. Rangan, L.H. Hurley, Selective interactions of cationic porphyrins with G-quadruplex structures, *J. Am. Chem. Soc.* 123 (37) (2001) 8902–8913.
- [18] L. Rossetti, M. Franceschin, A. Bianco, G. Ortaggi, M. Savino, Perylene diimides with different side chains are selective in inducing different G-quadruplex DNA structures and in inhibiting telomerase, *Bioorg. Med. Chem. Lett.* 12 (18) (2002) 2527–2533.
- [19] E.W. White, F. Tanious, M.A. Ismail, A.P. Reszka, S. Neidle, D.W. Boykin, W.D. Wilson, Structure-specific recognition of quadruplex DNA by organic cations: influence of shape, substituents and charge, *Biophys. Chem.* 126 (1) (2007) 140–153.
- [20] Y. Xue, Z.-y. Kan, Q. Wang, Y. Yao, J. Liu, Y.-h. Hao, Z. Tan, Human telomeric DNA forms parallel-stranded intramolecular G-quadruplex in K⁺ solution under molecular crowding condition, *J. Am. Chem. Soc.* 129 (36) (2007) 11185–11191.
- [21] G.N. Parkinson, M.P. Lee, S. Neidle, Crystal structure of parallel quadruplexes from human telomeric DNA, *Nature* 417 (6891) (2002) 876–880.
- [22] M.J. Frisch, G.W. Trucks, H.B. Schlegel, G.E. Scuseria, M.A. Robb, J.R. Cheeseman, J.A. Montgomery Jr., T. Vreven, K.N. Kudin, J.C. Burant, J.M. Millam, S.S. Iyengar, J. Tomasi, V. Barone, B. Mennucci, M. Cossi, G. Scalmani, N. Rega, G.A. Petersson, H. Nakatsuji, M. Hada, M. Ehara, K. Toyota, R. Fukuda, J. Hasegawa, M. Ishida, T. Nakajima, Y. Honda, O. Kitao, H. Nakai, M. Klene, X. Li, J.E. Knox, H.P. Hratchian, J.B. Cross, V. Bakken, C. Adamo, J. Jaramillo, R. Gomperts, R.E. Stratmann, O. Yazyev, A.J. Austin, R. Cammi, C. Pomelli, J.W. Ochterski, P.Y. Ayala, K. Morokuma, G.A. Voth, P. Salvador, J.J. Dannenberg, V.G. Zakrzewski, S. Dapprich, A.D. Daniels, M.C. Strain, O. Farkas, D.K. Malick, A.D. Rabuck, K. Raghavachari, J.B. Foresman, J.V. Ortiz, Q. Cui, A.G. Baboul, S. Clifford, J. Cioslowski, B.B. Stefanov, G. Liu, A. Liashenko, P. Piskorz, I. Komaromi, R.L. Martin, D.J. Fox, T. Keith, M.A. Al-Laham, C.Y. Peng, A. Nanayakkara, M. Challacombe, P.M.W. Gill, B. Johnson, W. Chen, M.W. Wong, C. Gonzalez, J.A. Pople, Gaussian 03, Revision C.02, Gaussian, Inc., Wallingford CT, 2004.
- [23] C.I. Bayly, P. Cieplak, W. Cornell, P.A. Kollman, A well-behaved electrostatic potential based method using charge restraints for deriving atomic charges: the RESP model, *J. Phys. Chem.* 97 (40) (1993) 10269–10280.
- [24] Y. Yang, J. Qin, H. Liu, X. Yao, Molecular dynamics simulation, free energy calculation and structure-based 3D-QSAR studies of B-Raf kinase inhibitors, *J. Chem. Inf. Model.* 51 (3) (2011) 680–692.
- [25] D.A. Case, T.E. Cheatham, T. Darden, H. Gohlke, R. Luo, K.M. Merz, A. Onufriev, C. Simmerling, B. Wang, R.J. Woods, The amber biomolecular simulation programs, *J. Comput. Chem.* 26 (16) (2005) 1668–1688.
- [26] A. Pérez, I. Marchán, D. Svozil, J. Sponer, T.E. Cheatham, C.A. Loughton, M. Orozco, Refinement of the AMBER force field for nucleic acids: improving the description of the ϵ/α conformers, *Biophys. J.* 92 (11) (2007) 3817–3829.
- [27] E. Fadrná, N.a. Špačková, J. Sarzynska, J. Koca, M. Orozco, T.E. Cheatham III, T. Kulinski, J. Sponer, Single stranded loops of quadruplex DNA as key benchmark for testing nucleic acids force fields, *J. Chem. Theory Comput.* 5 (9) (2009) 2514–2530.
- [28] J. Aqvist, Ion-water interaction potentials derived from free energy perturbation simulations, *J. Phys. Chem.* 94 (21) (1990) 8021–8024.
- [29] I.S. Joung, T.E. Cheatham, Determination of alkali and halide monovalent ion parameters for use in explicitly solvated biomolecular simulations, *J. Phys. Chem. B* 112 (30) (2008) 9020–9041.
- [30] J.-P. Ryckaert, G. Ciccotti, H.J. Berendsen, Numerical integration of the cartesian equations of motion of a system with constraints: molecular dynamics of n-alkanes, *J. Comput. Phys.* 23 (3) (1977) 327–341.
- [31] U. Essmann, L. Perera, M.L. Berkowitz, T. Darden, H. Lee, L.G. Pedersen, A smooth particle mesh Ewald method, *J. Chem. Phys.* 103 (19) (1995) 8577–8593.
- [32] A. Amadei, A. Linssen, H. Berendsen, Essential dynamics of proteins, *Proteins* 17 (1994) 412–425.
- [33] J. Mongan, Interactive essential dynamics, *J. Comput. Aid. Mol. Des.* 18 (6) (2004) 433–436.
- [34] W. Humphrey, A. Dalke, K. Schulten, VMD: visual molecular dynamics, *J. Mol. Graph.* 14 (1) (1996) 33–38.
- [35] O. Trott, A.J. Olson, AutoDock Vina: improving the speed and accuracy of docking with a new scoring function, efficient optimization, and multithreading, *J. Comput. Chem.* 31 (2) (2010) 455–461.
- [36] H. Gohlke, C. Kiel, D.A. Case, Insights into protein-protein binding by binding free energy calculation and free energy decomposition for the Ras-Raf and Ras-RalGDS complexes, *J. Mol. Biol.* 330 (4) (2003) 891–913.
- [37] D.A. Pearlman, D.A. Case, J.W. Caldwell, W.S. Ross, T.E. Cheatham, S. DeBolt, D. Ferguson, G. Seibel, P. Kollman, AMBER, a package of computer programs for applying molecular mechanics, normal mode analysis, molecular dynamics and free energy calculations to simulate the structural and energetic properties of molecules, *Comput. Phys. Commun.* 91 (1) (1995) 1–41.
- [38] Z. Wang, R. Chen, L. Hou, J. Li, J.-P. Liu, Molecular dynamics and principal components of potassium binding with human telomeric intra-molecular G-quadruplex, *Protein Cell* 6 (6) (2015) 423–433.
- [39] Z. Wang, J.P. Liu, Characterization of potassium binding with human telomeres, *Clin. Exp. Pharmacol.* 42 (9) (2015) 902–909.
- [40] N.V. Hud, F.W. Smith, F.A. Anet, J. Feigon, The selectivity for K⁺ versus Na⁺ in DNA quadruplexes is dominated by relative free energies of hydration: a thermodynamic analysis by 1H NMR, *Biochemistry-US* 35 (48) (1996) 15383–15390.
- [41] E. Gavathiotis, R.A. Heald, M.F.G. Stevens, M.S. Searle, Drug recognition and stabilisation of the parallel-stranded DNA quadruplex d(TTAGGGT)₄ containing the human telomeric repeat, *J. Mol. Biol.* 334 (1) (2003) 25–36.
- [42] N.H. Campbell, G.N. Parkinson, A.P. Reszka, S. Neidle, Structural basis of DNA quadruplex recognition by an acridine drug, *J. Am. Chem. Soc.* 130 (21) (2008) 6722–6724.
- [43] T. Mashimo, H. Yagi, Y. Sannohe, A. Rajendran, H. Sugiyama, Folding pathways of human telomeric type-1 and type-2 G-quadruplex structures, *J. Am. Chem. Soc.* 132 (42) (2010) 14910–14918.
- [44] S.M. Gowan, R. Heald, M.F. Stevens, L.R. Kelland, Potent inhibition of telomerase by small-molecule pentacyclic acridines capable of interacting with G-quadruplexes, *Mol. Pharmacol.* 60 (5) (2001) 981–988.
- [45] M. Laronze-Cochard, Y.M. Kim, B. Brassart, J.F. Riou, J.Y. Laronze, J. Sapi, Synthesis and biological evaluation of novel 4,5-bis(dialkylaminoalkyl)-substituted acridines as potent telomeric G-quadruplex ligands, *Eur. J. Med. Chem.* 44 (10) (2009) 3880–3888.
- [46] J.Q. Hou, S.B. Chen, J.H. Tan, T.M. Ou, H.B. Luo, D. Li, J. Xu, L.Q. Gu, Z.S. Huang, New insights into the structures of ligand-quadruplex complexes from molecular dynamics simulations, *J. Phys. Chem. B* 114 (46) (2010) 15301–15310.